



# Surface exploration of a room-temperature ionic liquid-chitin composite film decorated with electrochemically deposited PdFeNi trimetallic alloy nanoparticles by pattern recognition: An elegant approach to developing a novel biotin biosensor



Mohammad-Bagher Gholivand<sup>a,\*</sup>, Ali R. Jalalvand<sup>a,b</sup>, Hector C. Goicoechea<sup>b</sup>, Giti Paimard<sup>a</sup>, Thomas Skov<sup>c</sup>

<sup>a</sup> Faculty of Chemistry, Razi University, Kermanshah 671496734, Iran

<sup>b</sup> Laboratorio de Desarrollo Analítico y Quimiometría (LADAQ), Cátedra de Química Analítica I, Universidad Nacional del Litoral, Ciudad Universitaria, CC 242 (S3000ZAA) Santa Fe, Argentina

<sup>c</sup> Quality & Technology, Department of Food Science, Faculty of Science, University of Copenhagen, Copenhagen, Denmark

## ARTICLE INFO

### Article history:

Received 27 March 2014

Received in revised form

12 July 2014

Accepted 15 July 2014

Available online 8 August 2014

### Keywords:

Biotin

Chitin

Electrodeposition

Trimetallic alloy nanoparticles

Digital image processing

## ABSTRACT

In this study, a novel biosensing system for the determination of biotin (BTN) based on electrodeposition of palladium-iron-nickel (PdFeNi) trimetallic alloy nanoparticles (NPs) onto a glassy carbon electrode (GCE) modified with a room-temperature ionic liquid (RTIL)-chitin (Ch) composite film (PdFeNi/ChRTIL/GCE) is established. NPs have a wide range of applications in science and technology and their sizes are often measured using transmission electron microscopy (TEM) or X-ray diffraction. Here, we used a pattern recognition method (digital image processing, DIP) for measuring particle size distributions (PSDs) from scanning electron microscopic (SEM) images in the presence of an uneven background. Different depositions were performed by varying the number of cyclic potential scans ( $N$ ) during electroreduction step. It was observed that the physicochemical properties of the deposits were correlated to the performance of the PdFeNi/ChRTIL/GCE with respect to BTN assay. The best results were obtained for eight electrodeposition cyclic scans, where small-sized particles ( $19.54 \pm 6.27$  nm) with high density ( $682$  particles  $\mu\text{m}^{-2}$ ) were obtained. Under optimized conditions, a linear range from  $2.0$  to  $44.0 \times 10^{-9}$  mol  $\text{L}^{-1}$  and a limit of detection (LOD) of  $0.6 \times 10^{-9}$  mol  $\text{L}^{-1}$  were obtained. The PdFeNi/ChRTIL nanocomposite showed excellent compatibility, enhanced electron transfer kinetics, large electroactive surface area, and was highly sensitive, selective, and stable toward BTN determination. Finally, the PdFeNi/ChRTIL/GCE was satisfactorily applied to the determination of BTN in infant milk powder, liver, and egg yolk samples.

© 2014 Elsevier B.V. All rights reserved.

## 1. Introduction

Biotin (BTN, also called vitamin B6, B7 or H, Fig. 1) is a water-soluble vitamin and an essential co-factor for five BTN-dependent carboxylase enzymes. It is synthesized in a wide variety of bacteria and plants. However, several microorganisms as well as higher animals are notable to synthesize it and their needs in this vitamin are met by dietary intake [1]. Besides the typical clinical features, recent evidence indicates that the pregnant women develop BTN deficiency during normal pregnancy [2,3].

Although a maximum level of BTN in food is not specified, 1.5 mg in 100 kcal is recommended by the current regulation in infant formula in substitution of breast-milk to satisfy the nutritional requirements of infants during the first months of life [4]. Consequently, the diagnosis of BTN deficiency and the monitoring of its levels in patients receiving BTN treatment are important issues as well as its determination in foods and food supplement products. For this reason, analytical methods were developed in order to determine BTN in biological fluids as well as in food products and pharmaceutical preparations [5–10]. The analytical techniques for biotin determination can be divided into four main categories: (1) Microbiological methods, based on growth of microorganisms in presence of BTN, are very sensitive but they lack specificity and they are very time-consuming [11]. (2) Biological techniques are based on the animal development curve. These are used mainly for the determination of BTN in food [11]. (3) Binding

\* Corresponding author. Tel.: +98 831 4274557; fax: +98 831 4274559.

E-mail addresses: [mbgholivand2013@gmail.com](mailto:mbgholivand2013@gmail.com), [mbgholivand@yahoo.com](mailto:mbgholivand@yahoo.com) (M.-B. Gholivand).

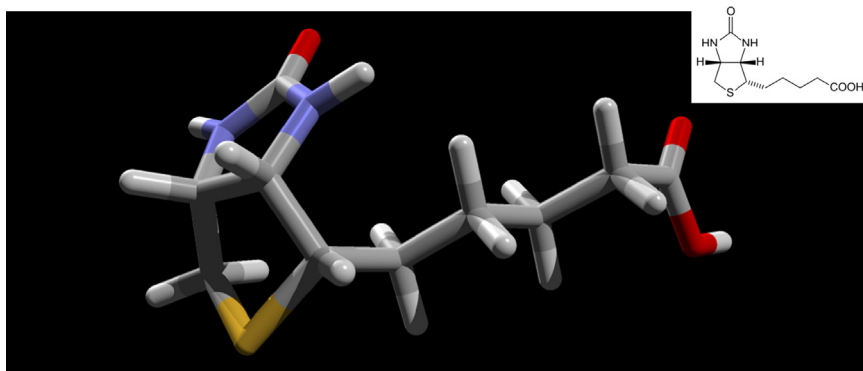


Fig. 1. Molecular structure of BTN.

assays make use of formation of a specific avidin (or streptavidin)–BTN complex [11]. (4) The last group of methods includes all physicochemical methods such as spectrophotometry, polarography, thin layer chromatography, gas chromatography, high performance liquid chromatography and capillary zone electrophoresis [11,12]. However, these methods suffer from some disadvantages such as high costs, long analysis times and requirement for sample pretreatment, and in some cases low sensitivity and selectivity that makes them unsuitable for routine analysis. To overcome these defects, electrochemical methods which are low costs are used extensively for the elegant and sensitive properties such as selectivity, simplicity, repeatability, and reproducibility [13–17].

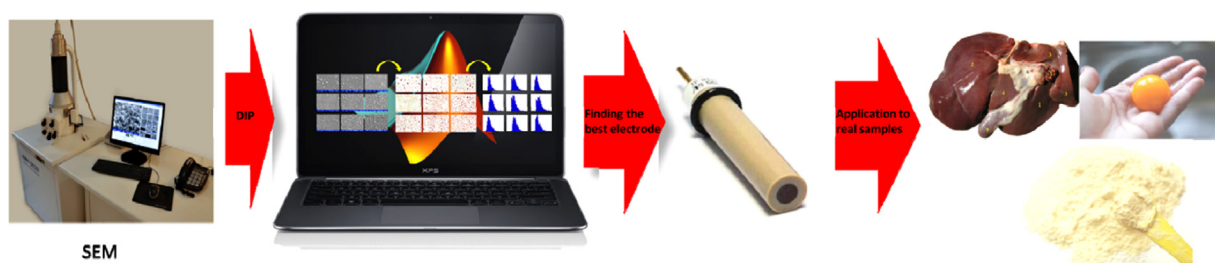
Chitin (Ch) is the second most abundant polysaccharide in biomass after cellulose with excellent film forming ability, biocompatibility, nontoxicity, good water permeability and high mechanical strength. Ch production was about 25,000 t in 2006 [18]. This polymer is a linear chain consisting of poly $\beta$ (1 $\rightarrow$ 4)*N*-acetyl-*D*-glucosamine. Ch is usually isolated from the exoskeletons of crustaceans and more particularly from shrimps and crabs where  $\alpha$ -chitin isomorph is produced [19]. Ch is largely widespread in biomass [20], and its main application is in the production of its water-soluble derivative chitosan. Ch and chitosan have exactly the same chemical structure, corresponding to the series of linear copolymers of (1 $\rightarrow$ 4)-2-amino-2-deoxy- $\beta$ -*D*-glucan and (1 $\rightarrow$ 4)-2-acetamido-2-deoxy- $\beta$ -*D*-glucan. Ch can accumulate metal ions through various mechanisms, such as chelation, electrostatic attraction, and ion exchange, depending on the nature of the metal ion and pH of the solution.

Room-temperature ionic liquids (RTILs) are liquid (molten) salts that exist for certain salts in a liquid state at and above room-temperature because of the particular kinds of interactions between certain cations and anions. In recent years, the research and development of RTILs to achieve the functions of low-flammability, low volatility, low-viscosity, and high electrochemical stability have been actively promoted [21–24]. Against such a background, applications such as various electrochemical devices (lithium secondary batteries [25–28], fuel cells [28,29], electric double-layer capacitors [30], dye-sensitized solar cells [31], field-effect transistors [32,33] etc.), tribology solvents [34], synthetic solvents [35], and biomass solvents [36] as functional uses of RTILs have been developed.

Nanoparticles (NPs) have been used extensively in the fields of physical, chemical and material sciences in the past few years [37]. These materials having a high specific surface area, large pore size and unique features, such as surface plasmon absorption, improved magnetic property, high reactivity, and enhanced catalytic activity [38]. They are also expected to show advantages for use as electrocatalysts due to their large active surface areas, small catalyst loading and abilities to prevent aggregation between particles [39]. Among the nanoparticles, metal nanoparticles are objects of great interest in modern chemistry and materials research, where they

find application in such diverse fields as photochemistry, nanoelectronics, optics, catalysis and electrocatalysis [40]. Their sizes are commonly linked directly to their catalytic activity, with different crystal nucleation and growth processes giving rise to different particle size distributions (PSDs). PSDs are measured routinely in industrial environments, with the requirement that they should be statistically meaningful. The adsorption technique for the determination of metal particle size is based on the fact that over an appropriate temperature range certain gases such as ethylene, carbon monoxide, oxygen and hydrogen form a chemisorbed monolayer on the surface of transition metals. It is an easy and simple experimental technique. The surface of the metal area can be inferred from the amount of adsorbed gas in combination with the metal content of the supported catalyst, only if assumptions are made about the particle shape (normally assumed to be spherical or cubic) [41]. The two complementary techniques that are typically used are X-ray diffraction and transmission electron microscopy (TEM). X-ray diffraction can be used to provide averaged information from large numbers of particles, but the interpretation of the results can be difficult, especially if the particles are not single crystals. TEM measurements rely on the acquisition of images and subsequent digital processing from typically no more than a few hundreds of particles [42,43]. However, even using digital image processing (DIP) tools, the quantification of the sizes and distributions of nanoparticles using TEM is difficult task. First, for supported catalysts, the particle sizes of interest are in the range of nanometers. The detection and analysis of small aggregates that are supported on amorphous or crystalline substrates is difficult, especially when the particle size approaches that of phase contrast arising from the support [44,45]. Second, this difficulty is exacerbated by the fact that the clusters may be present at different heights, they may be embedded in the support, they may be overlapped by other particles and the support itself may be thick or rough. Although the visibility of metal nanoparticles can often be enhanced by recording bright-field images slightly away from Gaussian focus, it is not possible to perform accurate size measurements from such images because the image resolution is then poorer. Inferences from bright-field TEM images are also complicated by diffraction effects, particularly as small particles possess large reciprocal-space shape functions that can be intersected by the Ewald sphere at large tilts from zone axes [46]. In order to provide statistically meaningful size distributions from scanning electron microscopy (SEM) images, many particles should be analyzed. Manual segmentation of SEM images can be time-consuming because, in most cases, it is difficult to analyze an image locally to obtain only the desired information from the particles. In order to address these issues, we are going to use DIP that makes use of a locally varying threshold.

Alloy NPs are widely used in catalysis and sensing fields. Owing to the interaction among components in alloy NPs, they generally show many favorable properties in comparison with the



**Scheme 1.** Schematic representation of the methodology employed to BTN assay.

corresponding monometallic counterparts, which include high catalytic activity, catalytic selectivity, and better resistance to deactivation [47]. Electrodeposition is the most controllable and robust technique for synthesis of metal NPs, in which the size, density, composition of alloys and even the shape of NPs can be well-controlled by electrodeposition potential, time, concentration, and composition of metal precursor solutions [48,49].

This paper presents a study concerning electrodeposition of PdFeNi trimetallic alloy NPs by cyclic voltammetry (CV) onto a glassy carbon electrode (GCE) modified with a room-temperature ionic liquid (RTIL)-chitin (Ch) composite film (PdFeNi/ChRTIL/GCE) aiming at BTN trace detection using differential pulse voltammetry (DPV) which has been reported for the first time. Different deposits were obtained by varying the number of cyclic potential scans during electroreduction step and we used a computerized method (DIP) for measuring PSDs from SEM images in the presence of an uneven background. Finally the sensitivity of the best resulting PdFeNi/ChRTIL/GCE sensor toward BTN assay was evaluated (Scheme 1).

## 2. Experimental and theoretical backgrounds

### 2.1. Experimental details

#### 2.1.1. Chemicals and solutions

1-Ethyl-3-methylimidazolium bis(trifluoromethylsulfonyl)imide (EMIMBTI), Ch, and BTN were purchased from Sigma-Aldrich. All other reagents were of analytical grade and used as received from Merck. A concentration of  $0.05 \text{ mol L}^{-1}$  phosphate buffered solution (PBS, prepared from  $\text{NaH}_2\text{PO}_4$  and  $\text{Na}_2\text{HPO}_4$ ) was used to control the pH at 4.0.  $[\text{Fe}(\text{CN})_6]^{3-/4-}$  solution (redox probe,  $5.0 \times 10^{-3} \text{ mol L}^{-1}$ ) was prepared in PBS ( $0.05 \text{ mol L}^{-1}$ , pH 4.0) and used for electrochemical impedance spectroscopic (EIS) measurements. A stock solution of BTN was prepared in PBS ( $0.05 \text{ mol L}^{-1}$ , pH 4.0) with a concentration level of  $0.01 \text{ mol L}^{-1}$ , and was stored at dark in a refrigerator. Working solutions were prepared by appropriate dilution of the stock solution. A stock solution of 0.2% Ch was prepared in 1.0% (v/v) acetic acid by ultrasonication for 30.0 min. Doubly distilled water ( $\text{ddH}_2\text{O}$ ) was used throughout the study.

#### 2.1.2. Apparatus and softwares

Electrochemical experiments were performed using a  $\mu$ -Auto-labIII/FRA2 controlled by the Nova software (Version 1.8). A conventional three-electrode cell was used with a saturated calomel electrode (SCE) as reference electrode, a Pt wire as counter electrode and a bare or modified GCE as working electrode. The EIS measurements were performed in the redox probe solution and plotted in the form of complex plane diagrams (Nyquist plots). The SEM experiments were performed by a KYKY-EM 3200 scanning electron microscope. A JENWAY-3345 pH-meter equipped with a combined glass electrode was used to pH measurements. Energy dispersive X-ray spectroscopy (EDS) was conducted by an EDS-integrated Hitachi S-4800 (Hitachi, Japan) for surface elemental

composition analysis. Digital image processing (DIP) was carried out using a MATLAB code and an adaptive thresholding algorithm for particles counting (density estimation) and average diameter measurement. The density and average size of PdFeNi NPs were evaluated from a  $6.1 \mu\text{m}^2$  GCE surface analysis. The recorded experimental data was smoothed, when necessary, and converted to matrices by means of several homemade MATLAB files. All computations were performed on a DELL XPS laptop (L502X) with Intel Core i7-2630QM 2.0 GHz, 8 GB of RAM and Windows 7-64 as its operating system.

#### 2.1.3. Preparation of the PdFeNi/ChRTIL/GCE

Prior to each modification, the GCE surface was polished successively by silicon carbide grinding paper (grit 1200.0) for 5.0 s, and by a 9.0, 5.0 and  $1.0 \mu\text{m}$  alumina slurry (Presi) on a cloth polishing pad for 10.0, 5.0 and 3.0 min, respectively. Between each polishing step, the surface was cleaned in an ultrasonic ethanol bath (5.0 min) in order to remove any impurity. Finally, they were rinsed in an ultrasonic  $\text{ddH}_2\text{O}$  bath (5.0 min) and dried for 1.0 min using a  $\text{N}_2$  stream. A distinct amount ( $15.0 \mu\text{L}$ ) of EMIMBTI was added to the Ch solution (0.2%,  $75.0 \mu\text{L}$ ) and with the aid of ultrasonic agitation a uniform solution (ChRTIL) was prepared. Then,  $4.0 \mu\text{L}$  of ChRTIL solution was dropped on the cleaned GCE and the solvent was evaporated by passing slow rate of warm air for 10.0 min. The electrochemical deposition of PdFeNi trimetallic alloy NPs was performed using CV on ChRTIL/GCE in  $0.2 \text{ mol L}^{-1}$  KCl solution containing  $0.5 \times 10^{-3} \text{ mol L}^{-1}$   $\text{PdCl}_2$ ,  $0.5 \times 10^{-3} \text{ mol L}^{-1}$   $\text{NiCl}_2$ , and  $0.5 \times 10^{-3} \text{ mol L}^{-1}$   $\text{FeCl}_3$  by scanning potential from 0 to  $-1 \text{ V}$  for a given number of scans ( $N$ ).

#### 2.1.4. Preparation of real samples

Three commercial infant formula milk powders (Aptamil, Similac and Bebelac), three pieces of Calf, Sheep and Chicken livers, and three Goose, Turkey and Chicken eggs were purchased from local markets. Before the experiments, the infant formula were mixed with 1.5% formic acid and then centrifuged for 10.0 min at 5000.0 rpm and the supernatant was collected for further sample assay [50]. Liver and egg yolk samples were incubated with  $2.25 \text{ mol L}^{-1}$  hydrochloric acid at  $100.0^\circ\text{C}$  for 120.0 min. Then, the samples were centrifuged for 10.0 min at 5000.0 rpm and the supernatants were filtered through a  $0.22 \mu\text{m}$  filter [51]. The filtrate was collected for further sample assay. The BTN concentration was ascertained from calibration curve and reported as  $\mu\text{g}$  BTN in  $100.0 \text{ g}$  sample.

### 2.2. Theoretical details

Image segmentation is an essential preliminary step in most automated pattern recognition and scene analysis problems [52]. Segmentation is used to subdivide an image into its constituent regions, and its accuracy determines the eventual success or failure of computerized analysis procedures. The detection of particles in a SEM image is usually performed by thresholding



the entire image at once using a single “global threshold” value. Individual pixels in the image are then marked as “object” pixels if their value is greater (or smaller) than a chosen threshold intensity and as “background” pixels otherwise. This approach works well if all of the particles have a sufficiently different intensity from that of the background. Once a binary (thresholded) image is obtained, an opening operator (erosion followed by dilation) can be used to smooth the boundaries by removing small protrusions, to break narrow isthmuses and to remove regions that are smaller than the size of a chosen

structuring element. Choosing the size of the kernel is possible to set a minimum size of particles to be detected. The image is then analyzed in order to measure and count the particles [53,54]. Unfortunately, in most cases of practical interest it is difficult to find a unique value for thresholding the entire picture correctly, and only a fraction of the particles in the image is outlined correctly in the binary image.

In order to address these issues, a method for improving the thresholding step before processing such images has been described [52]. The method is based on an “automatic local

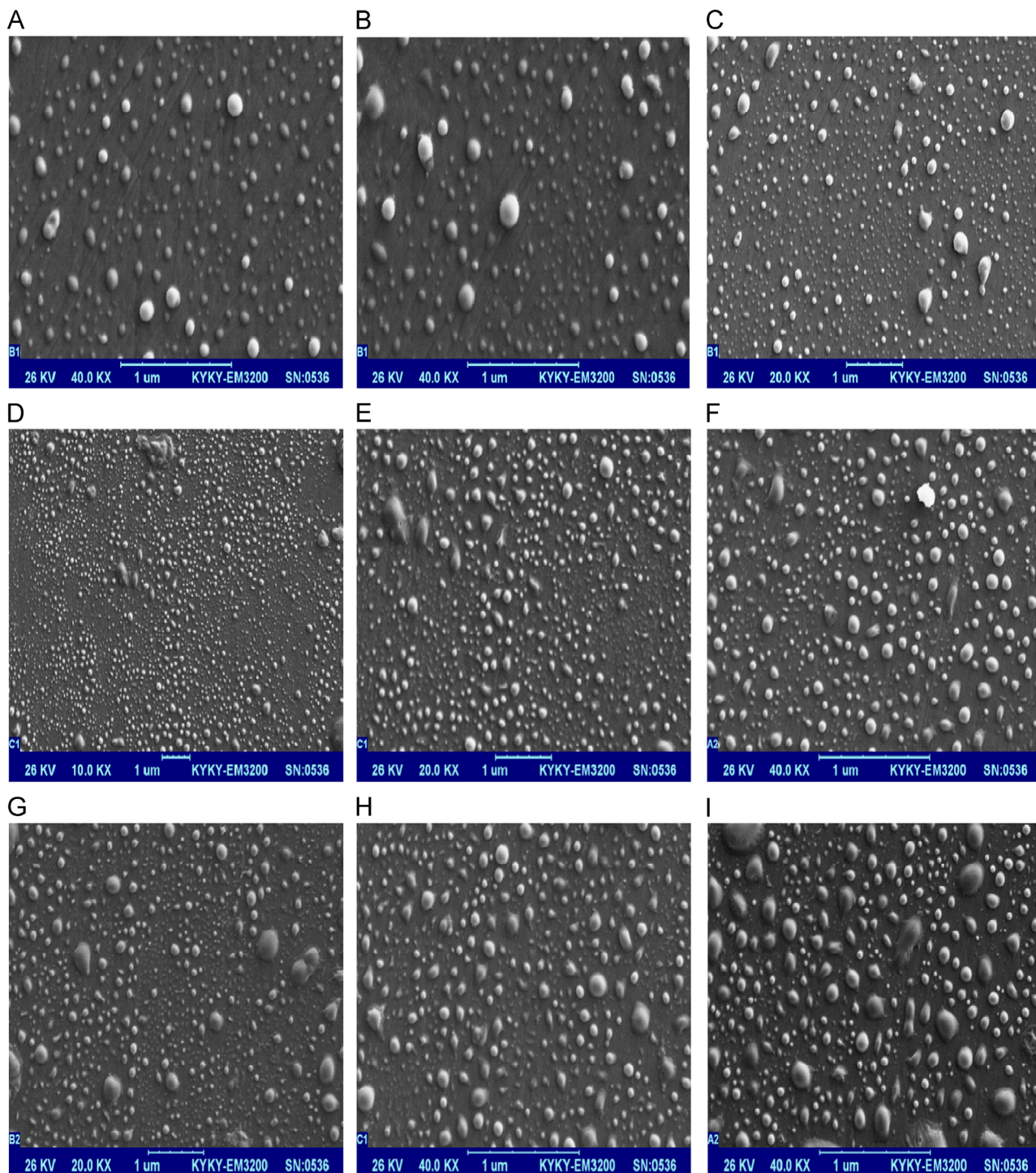


**Fig. 2.** SEM images of PdFeNi/ChRTIL/GCEs prepared by CV from a  $0.2 \text{ mol L}^{-1}$  KCl solution containing  $0.5 \times 10^{-3} \text{ mol L}^{-1}$   $\text{PdCl}_2$ ,  $0.5 \times 10^{-3} \text{ mol L}^{-1}$   $\text{NiCl}_2$  and  $0.5 \times 10^{-3} \text{ mol L}^{-1}$   $\text{FeCl}_3$  (see Section 2 for conditions). Number of cyclic scans ( $N$ ): (A) 1, (B) 2, (C) 4, (D) 8, (E) 12, (F) 16, (G) 20, (H) 24, and (I) 28.



thresholding” algorithm, which is applied to sub-regions of the image sequentially. The individual steps in the program include: (1) Selection of how many sub-divisions to use. (2) Cutting of sub-images from the original. (3) Thresholding of each sub-image. The output from this procedure is a binary image. (4) Opening (dilation plus erosion) with a chosen kernel size. (5) Combination and analysis of the processed sub-images. The resulting binary image is processed, particles counted and the boundaries are overlapped onto the original image to

check the results. The algorithm assumes that each sub-image to be thresholded contains two classes of pixels (e.g., foreground and background) and determines the optimal threshold automatically, in one of the several ways. The simplest way consists of (1) scaling the intensities in each sub-image and (2) selecting a threshold value equal to the median intensity range in each sub-image. After initial segmentation (e.g., using the mid-point between the minimum and the maximum intensities), the average of the intensities in each group of pixels

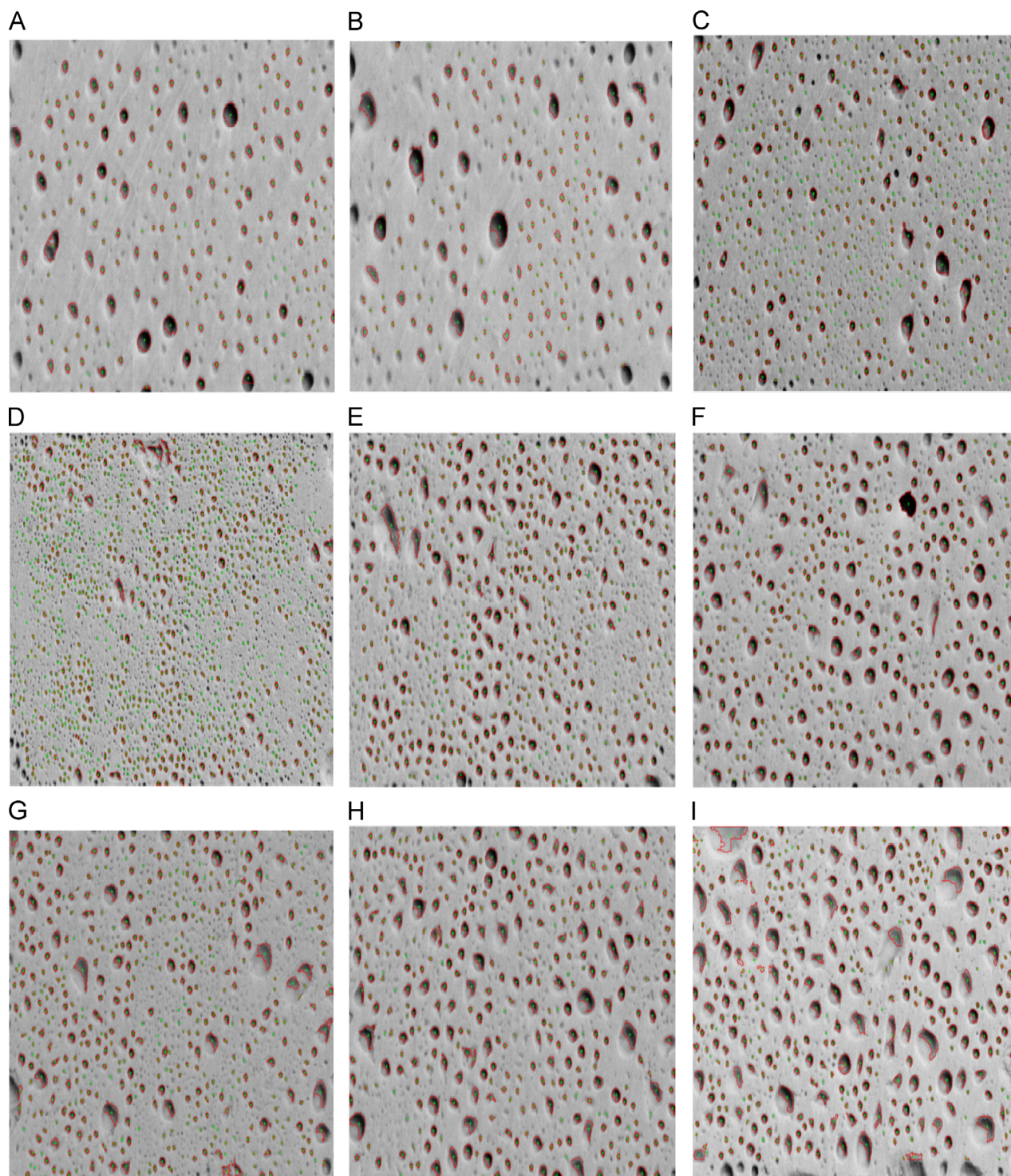


**Fig. 3.** The inversed images of the original SEM images presented in Fig. 1A–I processed by MATLAB image processing Toolbox.

is used to refine the threshold value. This procedure is repeated until the difference between successive threshold values is smaller than a pre-defined value. A more sophisticated approach, which is known as “Otsu’s method” can be used to determine the optimal threshold separating two classes of pixels so that the combined spread (intra-class variance) of the foreground and background pixels is minimized [55].

**Table 1**

Characterization of PdFeNi NPs for different number of cyclic scans ( $N$ ) during the electrodeposition step.

$N$	Number of NPs	NPs density (counts $\mu\text{m}^{-1}$ )	Mean diameter (nm)
1	1313	215	$22.48 \pm 10.42$
2	1440	236	$21.78 \pm 9.42$
4	1706	280	$21.50 \pm 9.57$
<b>8</b>	<b>4158</b>	<b>682</b>	<b><math>19.54 \pm 6.27</math></b>
12	2818	462	$19.68 \pm 7.88$
16	2371	389	$19.86 \pm 6.69$
20	2325	381	$20.18 \pm 8.24$
24	1927	316	$20.67 \pm 5.43$
28	1617	265	$21.29 \pm 5.20$

### 3. Results and discussion

#### 3.1. Electrodeposition of PdFeNi trimetallic alloy NPs onto ChRTIL/GCE

In this study, ChRTIL/GCE was chosen as a platform for electrodeposition of PdFeNi trimetallic alloy NPs. As suggested by other researchers, Ch can interact with the NPs, blocking the aggregation of NPs [56,57] and ILs have low interfacial tension and thus can enhance the nucleation rate, which is favorable to the formation of smaller NPs [58]. Nine ChRTIL/GCEs modified with PdFeNi trimetallic alloy NPs were elaborated using CV by scanning potential from 0 to  $-1$  V upon varying number of cyclic scans ( $N$ ) from 1.0 to 28.0.

#### 3.2. Characterizations

In order to characterize the PdFeNi trimetallic alloy NPs, SEM analyzes were carried out for nine significant values of  $N$  (Fig. 2A–I). For analyzing the SEM images by adaptive thresholding it was necessary to have a bright background with gray objects therefore, the original SEM images were loaded in MATLAB Workspace and inversed (Fig. 3A–I). The inversed SEM images were then submitted for analyzing by adaptive thresholding. As can be seen in Fig. 3A–I,

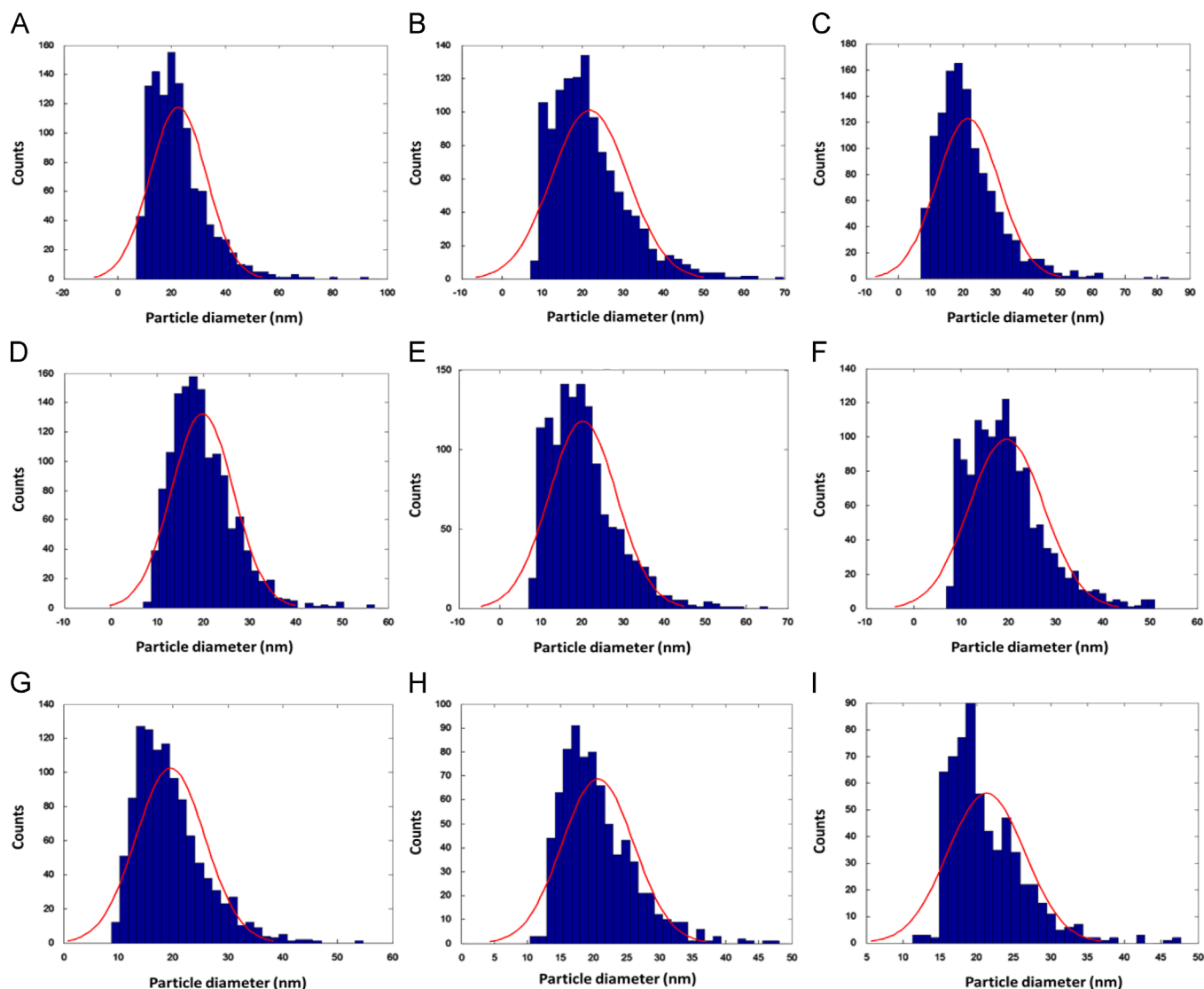


Fig. 4. Histograms of PSDs measured by DIP from the images presented in Fig. 2A–I.

the detected NPs were marked by pluses and surrounded by red circles. For the calculation of the particles size it was assumed the diameter of a circle with the same area as the particle. Table 1 summarizes the results obtained by DIP. Number of PdFeNi NPs, NPs densities, and mean diameters obtained by processing SEM images are reported in Table 1. Fig. 4A–I shows histograms of the measured PSDs for different applied  $N$ s and best-fitting curves. The electro-deposited PdFeNi NPs can be separated into two distinct populations: the first one is related to small and spherical-shaped NPs (Fig. 2A–F) and the second one to larger, aggregate-like NPs (Fig. 2G–I). An increase in the particles' densities as a function of  $N$  can be noticed up to eight potential scans, then the densities decreased (Table 1). By contrast, the average size of the particles decreased with respect to eight potential scans, then increased (Table 1). This evolution of both the density of PdFeNi NPs and the average size clearly illustrates a gradual coalescence phenomenon from  $N=8$ . However, while increasing  $N$  between 1 and 8 scans, small, and well spherical-shaped NPs formation is favored, and density reaches a maximum value at  $N=8$  and then decreases and NPs begin to coalesce, leading to larger NPs. Therefore,  $N=8$  was chosen as the best number of cyclic scans for the next measurements.

PdFeNi NPs were also characterized by energy dispersive X-ray spectroscopy (EDS) and signature peaks for Pd, Fe and Ni were observed (Fig. 5A). These peaks indicated that Pd, Fe and Ni can be electrochemically synthesized under the given conditions and contribute toward formation of trimetallic alloy NPs during the synthesis.

Electrochemical impedance spectroscopy (EIS) is an effective method for probing the features of surface of the modified electrodes. The Nyquist plot of impedance spectra includes a semicircle portion and a linear portion, with the former at higher frequencies corresponding to the electron transfer limited process and the latter at lower frequencies corresponding to the diffusion process. The electron transfer resistance ( $R_{ct}$ ) at the electrode surface is equal to the semicircle diameter, which can be used to describe the interface properties of the electrode. Fig. 5B displays the Nyquist plots of different electrodes in PBS (0.05 mol L<sup>-1</sup>, pH 4.0) containing  $5.0 \times 10^{-3}$  mol L<sup>-1</sup> [Fe(CN)<sub>6</sub>]<sup>3-/4-</sup>. It can be seen that the impedance curve of bare GCE (curve a) consists of a big semicircle, and the electron transfer resistance ( $R_{ct}$ ) is estimated to be 22.75 kΩ, whereas the  $R_{ct}$  of Ch/GCE (29.08 kΩ, curve b) is larger than that of bare GCE, manifesting that the Ch has a blocking effect on the electron transfer of [Fe(CN)<sub>6</sub>]<sup>3-/4-</sup>. When compared with Ch/GCE, ChRTIL/GCE exhibits a smaller  $R_{ct}$  (15.67 kΩ, curve c). This can be attributed to the good ionic conductivity of RTIL. In addition, the electrostatic interaction

between ChRTIL and [Fe(CN)<sub>6</sub>]<sup>3-/4-</sup> may favor the electron transfer of [Fe(CN)<sub>6</sub>]<sup>3-/4-</sup>. When the ChRTIL/GCE is coated with Fe (curve d), Ni (curve e), Pd (curve f), PdNi (curve h), FeNi (curve i), PdFe (curve g), and PdFeNi (curve j) NPs, the  $R_{ct}$  decreases 14.08, 8.55, 6.18, 5.34, 4.2, 3.25, and 2.29 kΩ, respectively. These results reveal that PdFeNi trimetallic alloy NPs can provide the necessary conduction pathways which cause better electron-transfer interface between electrode surface and electrolyte solution compared to monometallic or bimetallic NPs and also imply that there is a synergistic action between Pd, Fe, and Ni in decreasing electron transfer resistance.

Fig. 6 shows the CV responses for electrochemical oxidation of  $40.0 \times 10^{-9}$  mol L<sup>-1</sup> BTN in PBS (0.05 mol L<sup>-1</sup>, pH 4.0) at bare GCE (curve a), Ch/GCE (curve b), ChRTIL/GCE (curve c), Fe/ChRTIL/GCE (curve d), Ni/ChRTIL/GCE (curve e), Pd/ChRTIL/GCE (curve f), PdFe/ChRTIL/GCE (curve g), PdNi/ChRTIL/GCE (curve h), FeNi/ChRTIL/GCE (curve i) and PdFeNi/ChRTIL/GCE (curve j). As it can be seen, while the anodic peak potential for BTN oxidation at bare GCE, Ch/GCE, ChRTIL/GCE, are 1.21, 1.32, and 1.28 V, respectively, the corresponding potentials at Fe/ChRTIL/GCE, Ni/ChRTIL/GCE, Pd/ChRTIL/GCE, PdFe/ChRTIL/GCE, PdNi/ChRTIL/GCE, FeNi/ChRTIL/GCE, and PdFeNi/ChRTIL/GCE are 1.13, 1.18, 1.14, 1.08, 1.12, 1.18, and 1.07,

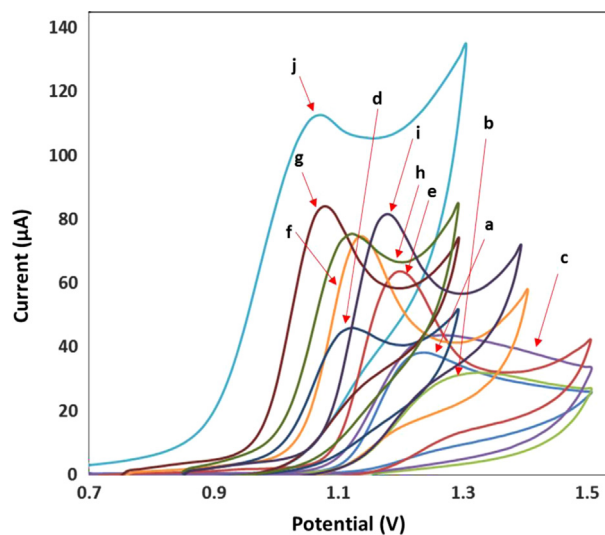


**Fig. 6.** CVs recorded at (a) bare GCE, (b) Ch/GCE, (c) ChRTIL/GCE, (d) Fe/ChRTIL/GCE, (e) Ni/ChRTIL/GCE, (f) Pd/ChRTIL/GCE (g) PdFe/ChRTIL/GCE, (h) PdNi/ChRTIL/GCE, (i) FeNi/ChRTIL/GCE and (j) PdFeNi/ChRTIL/GCE in the presence of 40.0 nM BTN in PBS (0.05 mol L<sup>-1</sup>, pH 4.0). Scan rate: 50.0 mV s<sup>-1</sup>.

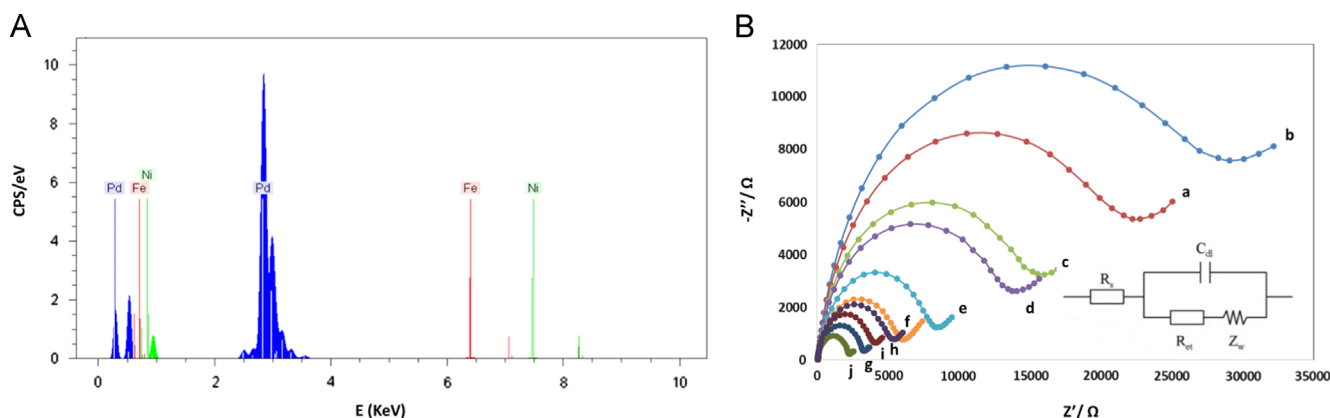


**Fig. 5.** (A) EDS spectra for confirming the presence of PdFeNi NPs on ChRTIL/GCE. (B) EIS spectra of (a) bare GCE, (b) Ch/GCE, (c) ChRTIL/GCE, (d) Fe/ChRTIL/GCE, (e) Ni/ChRTIL/GCE, (f) Pd/ChRTIL/GCE (g) PdFe/ChRTIL/GCE, (h) PdNi/ChRTIL/GCE, (i) FeNi/ChRTIL/GCE and (j) PdFeNi/ChRTIL/GCE in PBS (0.05 mol L<sup>-1</sup>, pH 4.0) containing  $5.0 \times 10^{-3}$  mol L<sup>-1</sup> [Fe(CN)<sub>6</sub>]<sup>3-/4-</sup>. Inset shows the equivalent circuit used for fitting the EIS data:  $R_s$ ,  $Z_w$ ,  $R_{ct}$  and  $C_{dl}$  represent the solution resistance, the Warburg diffusion resistance, the electron-transfer resistance and the double layer capacitance, respectively.



respectively. These results indicate that the peak potential for BTN oxidation at PdFeNi/ChRTIL/GCE shifts by 140.0 mV toward less positive values compared to bare GCE. However, PdFeNi/ChRTIL/GCE shows much higher anodic peak current for the oxidation of BTN compared to bare GCE, indicating that the combination of PdFeNi and ChRTIL has significantly improved the performance of the electrode toward BTN oxidation.

### 3.3. The influences of scan rate and pH on electrochemical response of BTN at PdFeNi/ChRTIL/GCE biosensor

The effect of scan rate ( $\nu$ ) on the electrocatalytic oxidation of BTN at PdFeNi/ChRTIL/GCE was investigated by CV (not shown). Results showed, the oxidation peak potential shifted to more positive potentials with increasing scan rate, confirming the kinetic limitation in the electrochemical reaction. Also, a plot of peak height ( $I_p$ ) vs. the square root of scan rate ( $\nu^{1/2}$ ) was found to be linear in the range of  $10\text{--}500\text{ mV s}^{-1}$  suggesting that the process is diffusion rather than surface controlled.

In general, pH is one of the variables, which commonly affects the current and shape of voltammograms. Taking into account that for analytical purposes both maximal and stable currents are necessary, the electrochemical behavior of BTN ( $0.05\text{ mol L}^{-1}$ ) in PBS

( $0.05\text{ mol L}^{-1}$ ) with various pHs (2.0–10.0) at the surface of PdFeNi/ChRTIL/GCE was studied using cyclic voltammetry (Fig. 7). This study showed that both peak current and peak potential depended on the solution pH. It can be seen that the anodic peak current of BTN reaches a maximum value at pH 4.0 and then decreases gradually with increasing of pH (inset of Fig. 7). Therefore, pH 4.0 was taken as the optimum pH for the determination of BTN. Also, the anodic peak potential of BTN at the surface of PdFeNi/ChRTIL/GCE shifts to less positive values with increasing pH of the buffered solution.

### 3.4. Analytical characterizations

Fig. 8 displays the differential pulse voltammetric (DPV) response of PdFeNi/ChRTIL/GCE biosensor for the successive increase in BTN concentrations. The calibration curve for the biosensor under the optimized experimental conditions is shown in the inset of Fig. 8. The biosensor exhibited a wide linear range of response to BTN, in the concentration range of  $2.0\text{--}44.0 \times 10^{-9}\text{ mol L}^{-1}$  with a correlation coefficient of 0.9973. The sensitivity of the biosensor was  $2.34\text{ }\mu\text{A nM}^{-1}$  and the limit of detection (LOD) was  $0.6 \times 10^{-9}\text{ mol L}^{-1}$ .

Long-term stability of the biosensor was also evaluated by measuring its performance after every few days. The biosensor shows high stability for BTN detection, and retains about 92% of its original response to BTN after 30.0 days of storage. These results suggest that the PdFeNi/ChRTIL/GCE possesses the long term stability. To ascertain the repeatability of the proposed biosensor, 10.0 measurements of  $10.0 \times 10^{-9}\text{ mol L}^{-1}$  BTN were carried out using the PdFeNi/ChRTIL/GCE at intervals of 1.0 h. The RSD was found to be 2.2%, indicating that the PdFeNi/ChRTIL/GCE has good repeatability. Six PdFeNi/ChRTIL/GCEs fabricated independently were used to determine  $10.0 \times 10^{-9}\text{ mol L}^{-1}$  BTN, and the RSD was 2.5%, revealing excellent reproducibility of the electrode preparation procedure. PdFeNi/ChRTIL/GCE biosensor can be prepared within 15.0 min and by manual polishing with alumina slurry we can retain the original nature of the GCE very easily.

The obtained results by the proposed biosensor with some reported methods [59–69] for the determination of BTN were compared and given in Table 2. The proposed biosensor provides better results over the most of the reported methods.

### 3.5. Interference study

Under optimal experimental conditions, the interference from selected metal ions and organic compounds was evaluated. The tolerance limit for interfering species was considered as the maximum concentration that gave a relative error less than  $\pm 5.0\%$

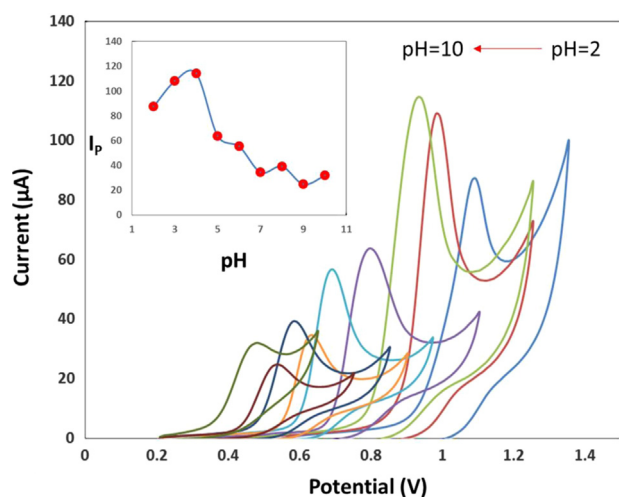


Fig. 7. Cyclic voltammograms for  $40.0 \times 10^{-9}\text{ mol L}^{-1}$  BTN on PdFeNi/ChRTIL/GCE (prepared by applying 8.0 cycles) in PBS ( $0.05\text{ mol L}^{-1}$ ) with pH values of 2.0–10.0.

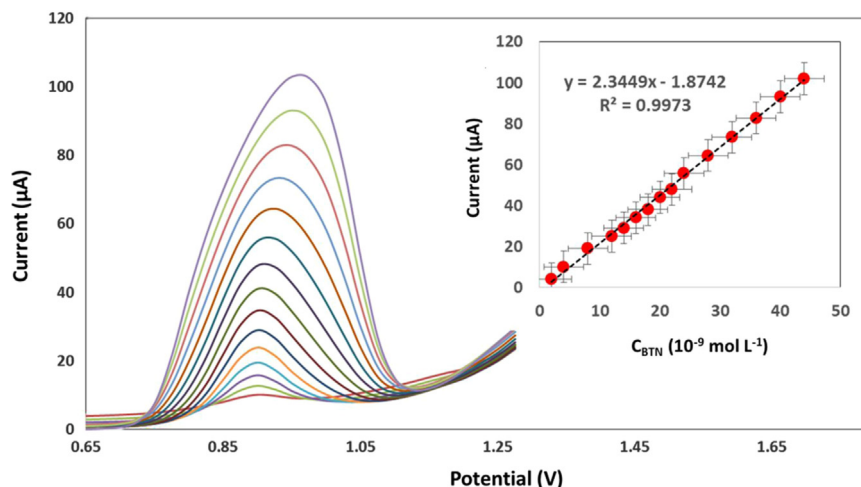


Fig. 8. Differential pulse voltammograms of PdFeNi/ChRTIL/GCE (prepared by applying 8.0 cycles) in PBS ( $0.05\text{ mol L}^{-1}$ , pH 4.0) containing  $2.0\text{--}44.0 \times 10^{-9}\text{ mol L}^{-1}$  BTN from inside to outside. Inset shows linear dependence of peak currents on BTN concentrations as calibration curve.

**Table 2**  
Electrochemical methods for BTN determination.

Technique	Method description	Linear range (mol L <sup>-1</sup> )	LOD (mol L <sup>-1</sup> )	Original applications	Ref.
HPLC- <sup>a</sup> SWV	Avidin-modified electrode	0–2 × 10 <sup>-6</sup>	1.3 × 10 <sup>-6</sup>	Pharmaceutical drug	[59]
<sup>b</sup> QCM sensor	Avidin immobilized on the crystal surface	7 × 10 <sup>-8</sup> –7 × 10 <sup>-6</sup>	7 × 10 <sup>-8</sup>	Pharmaceutical drug	[60]
<sup>c</sup> DPV	Competition between BTN and labeled BTN with daunomycin	3 × 10 <sup>-9</sup> –5 × 10 <sup>-8</sup>	3 × 10 <sup>-8</sup>	Pharmaceutical drug	[61]
DPV	Competition between BTN and labeled BTN with daunomycin	–	2 × 10 <sup>-9</sup>	Pharmaceutical drug	[62]
DPV	Competition between BTN and labeled BTN with Nile Blue A	3 × 10 <sup>-10</sup> –5 × 10 <sup>-8</sup>	1 × 10 <sup>-9</sup>	Vitamin tablet	[63]
Amperometry	Competition between BTN and biotinylated glucose oxidase	2.86 × 10 <sup>-7</sup> –8.19 × 10 <sup>-6</sup>	2.86 × 10 <sup>-7</sup>	Vitamin tablet	[64]
Amperometry	Anti-BTN antibody immobilized in electrode and BTN-HRP	4.09 × 10 <sup>-8</sup> –1.23 × 10 <sup>-5</sup>	4.09 × 10 <sup>-8</sup>	Vitamin tablet	[65]
SWV	Anti-BTN antibody immobilized in screen printed electrode using K <sub>4</sub> Fe(CN) <sub>6</sub> as electroactive substance	10 <sup>-6</sup> –10 <sup>-9</sup>	1.4 × 10 <sup>-8</sup>	Vitamin tablet	[66]
SWV	Electrochemical magneto biosensor	0.94–2.4 × 10 <sup>-7</sup>	8.4 × 10 <sup>-8</sup>	Dietary supplement and milk powder	[67]
Chromatography	HPLC-MS/MS	2 × 10 <sup>-9</sup> –2 × 10 <sup>-7</sup>	2 × 10 <sup>-9</sup>	Vitamin tablet	[68]
Chromatography	Postcolumn derivatization with <i>o</i> -phthalaldehyde and 3-mercaptopropionic acid	4.1 × 10 <sup>-6</sup> –4.1 × 10 <sup>-5</sup>	2 × 10 <sup>-6</sup>	Pharmaceutical preparations	[69]
DPV	PdFeNi/ <sup>d</sup> ChRTIL/GCE	2.0–44.0 × 10 <sup>-9</sup>	6 × 10 <sup>-10</sup>	Milk powder, liver, and egg yolk	This work

<sup>a</sup> SWV: Square wave voltammetry.<sup>b</sup> QCM: Quartz crystal microbalance.<sup>c</sup> DPV: Differential pulse voltammetry.<sup>d</sup> Chitin room temperature ionic liquid.**Table 3**  
Results of determination of BTN in real samples.

Sample	Found (μg 100 g <sup>-1</sup> )	Added (μg 100 g <sup>-1</sup> )	Found (μg 100 g <sup>-1</sup> )	Recovery (%)	RSD (% , n=3)
Milk powder (Aptamil) <sup>a</sup>	38.2	15.0	55.4	103.97	3.31
Milk powder (Similac) <sup>b</sup>	63.4	10.0	71.1	96.87	2.82
Milk powder (Bebelac) <sup>c</sup>	7.11	20.0	27.6	101.77	4.15
Calf liver	218.2	30.0	252.3	101.62	1.88
Sheep liver	231.9	25.0	258.5	100.61	2.43
Chicken liver	182.5	12.0	195.3	100.4	3.21
Goose egg yolk	18.6	6.0	24.2	98.38	3.666
Turkey egg yolk	28.4	14.0	41.6	98.12	2.71
Chicken egg yolk	31.3	15.0	47.2	101.90	2.55

<sup>a</sup> Labeled 40 μg 100 g<sup>-1</sup>.<sup>b</sup> Labeled 60 μg 100 g<sup>-1</sup>.<sup>c</sup> Labeled 6.5 μg 100 g<sup>-1</sup>.

at a concentration of  $10.0 \times 10^{-9}$  mol L<sup>-1</sup> of BTN. Phenol, ascorbic acid, caffeine, uric acid, glucose, citric acid, urea, cysteine, arginine, lysine, and aspartic acid were the most common constituents found with BTN. From the studies, an 80-fold excess of ascorbic acid had no effect on the  $I_p$  of BTN. Glucose, cysteine, arginine, lysine, aspartic acid, uric acid, citric acid and urea also did not interfere until a 100-fold excess was achieved. In addition, phenol, and caffeine showed no changes in  $I_p$  until a 70-fold excess was used. Even a 200-fold excess of K<sup>+</sup>, Ca<sup>2+</sup>, NO<sub>3</sub><sup>-</sup>, NH<sub>4</sub><sup>+</sup>, Cl<sup>-</sup> or Mg<sup>2+</sup> had no effect on the  $I_p$  of BTN. These results suggested that the determination of BTN at PdFeNi/ChRTIL/GCE biosensor was not significantly affected by the most common interfering species.

### 3.6. Real sample analysis

To evaluate the feasibility of the proposed biosensing system in real sample analysis, it was applied to the determination of BTN in infant milk powder, liver, and egg yolk samples, and the results are shown in Table 3. For the accuracy studies, a recovery study was carried out and the recovery values were between 96.87% and 103.97%. The RSD values were lower than 4.9% which confirmed

that acceptable values were also obtained for RSDs. Moreover, the differences between the results of this work for BTN determination in infant milk powders and the nominal values labeled by the manufacturer companies are small (see Table 3). These results suggested that the PdFeNi/ChRTIL/GCE biosensor was very reliable and sensitive enough for the determination of BTN in real samples.

## 4. Conclusions

For the first time we are reporting a simple method based on CV assisted by DIP for electrodeposition of PdFeNi trimetallic alloy NPs onto ChRTIL/GCE to fabricate a novel biosensor for efficient determination of BTN in real samples. Although not often used, CV proved to be an efficient method for spherical-like shaped NPs electrodeposition. The systematic characterization of the electrodes using CV and SEM for different values of *N* allowed a correlation to be made between both PdFeNi NPs density and size and the performances of the biosensor toward BTN detection. Measurement of PSDs from SEM images is difficult, especially on an uneven background. Therefore, this problem was tackled by

partitioning SEM micrographs into sub-images automatically and segmenting them using an adaptive threshold referred to as Otsu's method. Using this approach, images are analyzed with little human intervention and more accurately and objectively than when using a global threshold. PdFeNi/ChRTIL/GCE exhibits interesting performances with respect to BTN trace determination, and the best electrochemical responses were obtained for a high density (682 particles  $\mu\text{m}^{-2}$ ) of small NPs ( $19.54 \pm 6.27$  nm). From those observations, both NPs density and diameter appeared to be key features with respect to analytical performances. The proposed biosensor was sensitive, selective, free of common interferences with the analyte of interest, and had a sub-nanomolar detection limit. This biosensor is recommended for the determination of BTN at trace levels in quality control laboratories.

## Acknowledgements

The financial supports of this project by Razi University Research Council, UNL, CONICET and ANPCyT are gratefully acknowledged. We wish to express our sincere thanks and appreciation both to Mr. Abdolhamid Rezaee (SEM Operator) who provided the SEM images of our electrodes.

## References

- [1] E. Livaniou, D. Costopoulou, I. Vassiliadou, L. Leondiadis, J.O. Nyalala, D.S. Ithakissios, G.P. Evangelatos, J. Chromatogr. A 881 (2000) 331–343.
- [2] C.G. Staggs, W.M. Sealey, B.J. McCabe, A.M. Teague, D.M. Mock, J. Food Compos. Anal. 17 (2004) 767–776.
- [3] R.J. Stratton, T.R. Smith, Best Pract. Res. Clin. Gastroenterol 20 (2006) 441–466.
- [4] Código Alimentario Argentino based on Codex Alimentarius Commission, 2007. Standards for Infant Formulas and Formulas for Special Medical Purposes Intended for Infants (Codex Stan 72-1981) (Revised 2007).
- [5] H. Martin, C. Murray, J. Christeller, T. McGhie, Anal. Biochem. 381 (2008) 107–112.
- [6] S. Tanaka, K. Yoshida, H. Kuramitz, K. Sugawara, H. Nakamura, Anal. Sci. 15 (1999) 863–866.
- [7] L. Thompson, D. Schmitz, S. Pan, J. AOAC Int. 89 (2006) 1515–1558.
- [8] R. Kizek, M. Masarik, K.J. Kramer, D. Potesil, M. Bailey, J.A. Howard, B. Klejdus, R. Mikelova, V. Adam, L. Trnkova, F. Jelen, Anal. Bioanal. Chem. 381 (2005) 1167–1178.
- [9] T. Deng, J. Li, S. Huan, H. Yang, H. Wang, G. Shen, R. Yu, Biosens. Bioelectron. 21 (2006) 1545–1552.
- [10] J.M. Fowler, D.K.Y. Wong, H.B. Halsall, W.R. Heineman, Recent developments in electrochemical immunoassays and immunosensors, in: X. Zhang, H. Ju, J. Wang (Eds.), Electrochemical Sensors, Biosensors and their Biomedical Applications, Elsevier Inc., Amsterdam, 2008, pp. 115–143.
- [11] E. Livaniou, D. Costopoulou, I. Vassiliadou, L. Leondiadis, J.O. Nyalala, D.S. Ithakissios, G.P. Evangelatos, J. Chromatogr. A 881 (2000) 331–343.
- [12] J. Schiewe, S. Gobel, M. Schwarz, R. Neubert, J. Pharm. Biomed. Anal. 14 (1996) 435–439.
- [13] Y. Ikariyama, M. Furuki, M. Aizawa, Anal. Chem. 57 (1985) 496–500.
- [14] F. Delgado Reyes, J.M. Fernández Romero, M.D. Luque de Castro, Anal. Chim. Acta 436 (2001) 109–117.
- [15] Y. Gao, F. Guo, S. Gokavi, A. Chow, Q. Sheng, M. Guo, Food Chem. 110 (2008) 769–776.
- [16] R.M. Stuetz, Application of electronic nose technology for monitoring water and wastewater, in: S. Alegret (Ed.), Comprehensive Analytical Chemistry, Elsevier B.V., Amsterdam, 2003.
- [17] A. Lermo, S. Fabiano, S. Hernández, R. Galve, M.P. Marco, S. Alegret, M.I. Pividori, Biosens. Bioelectron. 24 (2009) 2057–2063.
- [18] M. Zhang, A. Smith, W. Gorski, Anal. Chem. 76 (2004) 5045–5050.
- [19] X. Lu, Z. Wen, J. Lin, Biomaterials 27 (2006) 5740–5747.
- [20] J. Lin, W. Qu, S. Zhang, Anal. Biochem. 360 (2007) 288–293.
- [21] M. Koel, Crit. Rev. Anal. Chem. 35 (2005) 177–192.
- [22] M. Rantwijk, R.A. Sheldon, Chem. Rev. 107 (2005) 2757–2785.
- [23] M. Haumann, A. Riisager, Chem. Rev. 108 (2008) 1474–1497.
- [24] M.A.P. Martins, C.P. Frizzo, D.N. Moreira, N. Zantta, H.G. Bonacorso, Chem. Rev. 108 (2008) 2015–2050.
- [25] H. Sakaebe, H. Matsumoto, Electrochem. Commun. 5 (2003) 594–598.
- [26] M. Ishikawa, T. Sugimoto, M. Kikuta, E. Ishiko, M. Kono, J. Power Sources 162 (2006) 658–662.
- [27] S. Seki, Y. Kobayashi, H. Miyashiro, Y. Ohno, Y. Mita, A. Usami, N. Terada, M. Watanabe, Electrochem. Solid-State Lett. 8 (2005) 577–578.
- [28] A. Noda, M.A.B.H. Susan, K. Kudo, S. Mitsushima, K. Hayamizu, M. Watanabe, J. Phys. Chem. B 107 (2003) 4024–4033.
- [29] R. Hagiwara, T. Nohira, K. Matsumoto, Y. Tamba, Electrochem. Solid-State Lett. 8 (2005) 231–233.
- [30] M. Ue, M. Takeda, T. Takahashi, M. Takehara, Electrochem. Solid-State Lett. 5 (2002) 119–121.
- [31] D. Kuang, P. Wang, S. Ito, S.M. Zakeeruddin, M. Gratzel, J. Am. Chem. Soc. 128 (2006) 7732–7733.
- [32] J. Lee, M.J. Panzer, Y. He, T.P. Lodge, C.D. Frisbie, J. Am. Chem. Soc. 129 (2007) 4532–4533.
- [33] S. Ono, S. Seki, R. Hirahara, Y. Tominari, J. Takeya, Appl. Phys. Lett. 92 (2008) 103313 (103313).
- [34] R.D. Rogers, K.R. Seddon, Science 302 (2003) 792–793.
- [35] P. Wasserscheid, W. Keim, Angew. Chem. Int. Ed. 39 (2000) 3772–3789.
- [36] Y. Fukaya, K. Hayashi, M. Wada, H. Ohno, Green Chem. 10 (2008) 44–46.
- [37] M. Dienerowitz, M. Mazilu, K. Dholakia, J. Nanophoton. 2 (2008) (art.no. 021875).
- [38] P.K. Jain, X. Huang, I.H. El-Sayed, M.A. El-Sayed, Plasmonics 2 (2007) 107–118.
- [39] F.W. Campbell, R.G. Compton, Anal. Bioanal. Chem. 396 (2010) 241–259.
- [40] K. Watanabe, D. Menzel, N. Nilius, H.J. Freund, Chem. Rev. 106 (2006) 4301–4320.
- [41] C.R. Adams, H.A. Benesi, R.M. Curtis, R.G. Meisenheimer, J. Catal. 1 (1962) 336–344.
- [42] M.T. Reetz, M. Maase, T. Schilling, B. Tesche, J. Phys. Chem. B 104 (2000) 8779–8781.
- [43] D.M. Rubin, J. Sediment Res. 74 (2004) 160–165.
- [44] K. Heinemann, F. Soria, Ultramicroscopy 20 (1986) 1–14.
- [45] M.J. Hytch, M. Gandais, Philos. Mag. A 72 (1995) 619–634.
- [46] M.M.J. Treacy, A. Howie, J. Catal. 63 (1980) 265–269.
- [47] A. Safavi, F. Farjami, Biosens. Bioelectron. 26 (2011) 2547–2552.
- [48] J.C. Claussen, A.D. Franklin, A. ul Haque, D.M. Porterfield, T.S. Fisher, ACS Nano 3 (2009) 37–44.
- [49] J. Yang, W.D. Zhang, S. Gunasekaran, Biosens. Bioelectron. 26 (2010) 279–284.
- [50] S.V. Kergaravat, G.A. Gomez, S.N. Fabiano, T.I.L. Chavez, M.I. Pividori, S.R. Hernandez, Talanta 97 (2012) 484–490.
- [51] V. Roman-Pizarro, J.M. Fernandez-Romero, A. Gomez-Hens, Talanta 99 (2012) 538–543.
- [52] L.C. Gontard, D. Ozkaya, R.E. Dunin-Borkowski, Ultramicroscopy 111 (2011) 101–106.
- [53] J.C. Russ, The Image Processing Handbook, CRC Press Inc., Boca Raton, FL, USA, 2002.
- [54] R.C. Gonzalez, R.E. Woods, Digital Image Processing, Prentice Hall, 2002.
- [55] N. Otsu, IEEE Trans. Syst. Man Cybern. 9 (1979) 62–66.
- [56] P. Sorlier, A. Denuziere, C. Viton, A. Domard, Biomacromolecules 2 (2001) 765–772.
- [57] H. Huang, Q. Yuan, X. Yang, Colloids Surf., B 39 (2004) 31–37.
- [58] F. Xiao, F. Zhao, Y. Zhang, G. Guo, B. Zeng, J. Phys. Chem. C 113 (2009) 849–855.
- [59] R. Kizek, M. Masarik, K.J. Kramer, D. Potesil, M. Bailey, J.A. Howard, B. Klejdus, R. Mikelova, V. Adam, L. Trnkova, F. Jelen, Anal. Bioanal. Chem. 381 (2005) 1167–1178.
- [60] T. Deng, J. Li, S. Huan, H. Yang, H. Wang, G. Shen, R. Yu, Biosens. Bioelectron. 21 (2006) 1545–1552.
- [61] K. Sugawara, S. Tanaka, H. Nakamura, Anal. Chem. 67 (1995) 299–302.
- [62] S. Tanaka, F. Yamamoto, K. Sugarwara, H. Nakamura, Talanta 44 (1997) 357–363.
- [63] K. Sugawara, Y. Yamauchi, S. Hoshi, K. Akatsuka, F. Yamamoto, S. Tanaka, H. Nakamura, Bioelectrochem. Bioenerg. 41 (1996) 167–172.
- [64] J. Wright, K. Rawson, Biosens. Bioelectron. 10 (1995) 495–500.
- [65] B. Lu, E.I. Iwuoha, M.R. Smyth, R. O'Kennedy, Anal. Chim. Acta 345 (1997) 59–66.
- [66] J. Ho, W. Hsu, W. Liao, J. Chiu, M. Chen, H. Chang, C. Li, Biosens. Bioelectron. 26 (2010) 1021–1027.
- [67] S.V. Kergaravat, G.A. Gómez, S.N. Fabiano, Tamara I. Laube Chávez, M.I. Pividori, S.R. Hernández, Talanta 97 (2012) 484–490.
- [68] U. Holler, F. Wächter, C. Wehrli, C. Fizez, J. Chromatogr. B 831 (2006) 8–16.
- [69] S. Nojiri, K. Kamata, M. Nishijima, J. Pharm. Biomed. 16 (1998) 1357–1362.